UNIVERSITY OF COPENHAGEN
FACULTY OF SCIENCE

University of Copenhagen

BSc Physics

Bachelor's Thesis

Revised edition
January 2021

Lazar Lakic KU- ID: mjx381

Two-chip quantum devices: Development and coupling of NbTiN microwave resonators to InAs nanowire devices

Advisor : Ferdinand Kuemmeth

NAME OF INSTITUTE: Niels Bohr Institute

NAME OF DEPARTMENT: Center for quantum devices

AUTHOR: Lazar Lakic

EMAIL: mjx381@alumni.ku.dk

TITLE: Two-chip quantum devices

SUPERVISOR: Ferdinand Kuemmeth

HANDED IN: 20.Jan.2021

Defended: xx.xx.2021

Name: _____

Signature:_____

Date:_____

Abstract

This thesis studies the combination and coupling of a bosonic and a fermionic quantum system. Namely, we explore the juxtaposition of a Niobium Titanium Nitride (NbTiN) superconducting resonator and an Indium Arsenide (InAs) nanowire (NW) double quantum dot device, with the aim of using the resonator to perform dispersive readout measurements of the quantum dot and working towards strong light-matter coupling of a microwave photon and an electron spin. The project at its core is twofold. On one hand, we present characterization and development of NbTiN superconducting high-kinetic- inductance resonators. On the other hand, we show progress towards a fabrication process for an InAs NW device coupled to a resonator, focusing on NW deposition and achieving an optimal quantum dot gate design to use in combination with the galvanically coupled readout resonators located both on and off chip.

Concretely, we measure and compare the loaded quality factors of coupled, uncoupled, on-chip and off-chip resonators with various design specifics. We include a discussion of both resonator and nanowire device fabrication, detailing success, failure and improvement pathways, on the basis of which we envision a future attempt to achieve strong couplin in these hybrid systems. The outlook of the project is to study various quantum phenomena, such as spin to spin coupling over *mm*-scale distances, for example between two separate chips, or to study spin dynamics in quantum dot systems with microsecond-scale readout times provided by dispersively coupled resonators [1, 2].

I would like to dedicate this thesis to my dear friend Daryoush Rahmanzadeh.

† 5. June. 1956 - 7. March. 2021 †

Contents

1 Introduction

Superconducting microwave resonators are becoming an essential component for many subfields of quantum computing and information, where they can provide the ability to measure and couple quantum information in various qubit systems [3]. This subfield goes under the name of circuit quantum electrodynamics (cQED) and is very much analogous to the manipulation of atoms in optical photon cavities - just with artificial atoms, and micro/radio waves instead of optical photons. While cQED since the late 80s has shown great success with various superconducting qubit platforms [4, 5], it has started showing promise in the field of superconductor-semiconductor ("super-semi") hybrid systems in the last 10 years [6, 1].

A problem for super-semi systems can be their need for several external control parameters, in the form of voltage controlled electrodes introducing excess photon losses. Additionally, some spin qubit platforms and various experiments for the detection of Majorana fermions require the use of magnetic fields [1, 7]. Magnetic fields pose a problem for ordinary superconducting resonators as the fields induce supercurrent vortices that interfere with the resonator photons, causing dissipation. We wish to combat this with the high quality factors of Niobium Titanium Nitride (NbTiN) thin film microstrip resonators that show strong resilience against magnetic fields [8].

The superconducting resonators can be used with quantum dots in two regimes, namely the dispersive (many photon) regime and the strong coupling (few photon) regime [6]. Achieving strong coupling of photon and electron spin is an important milestone for transporting information between multiple quantum devices [1].

In this thesis, we wish to test the use of NbTiN resonators for dispersive readout. This is done by using the resonator in its many-photon regime to sense small capacitive changes of systems with a low density-of-states, such as two-dimensional electron gases (2DEGs), or the system described in this thesis, InAs semiconducting NWs. Specifically, we use both "on chip" and "off chip" NbTiN superconducting microwave resonators and couple them to InAS NW quantum dots. We use InAs NWs as they provide us a fabrication process with fewer fabrication steps than lateral gated 2DEG dots, while also having a pronounced spin-orbit coupling (relevant for more exotic experiments involving Majorana fermions in future experiments) and posses favorable confinement properties due to their low effective electron mass [9].

Furthermore, we also work towards reaching the strong coupling of photon and electron spin, by improving our resonator design to enhance our quality factor and the coupling between the two systems. Eventually, for these nanowire-resonator systems, the goal is to achieve the quantum hybridization of photon and electron-spin, as described by the theoretical framework of the Jaynes-Cummings (JC) model [10].

2 Readout resonators, light-matter interaction and quantum dots

2.1 cQED and dispersive readout

The cQED framework relies on the use of microwave photon resonators to measure and couple quantum information embedded in 'matter' [11, 12]. It builds on the principle that the 'atom' (in our case, the dipole of an electron in a artificial atom) under investigation couples energetically to the photon from a harmonic oscillator [11, 12]. This is described by the Jaynes-Cummings Hamiltonian [12], which is a simple model of a photon coupling to a two level system

$$H_{JC} = \hbar\omega_r(a^\dagger a + 1/2) + 1/2\hbar\omega_d\sigma_z + \hbar g(\sigma_+ a + a^\dagger\sigma_-). \tag{1}$$

The first term $\hbar\omega_r(a^\dagger a + 1/2)$ is the harmonic-oscillator-like excited states of the photon, ω_r being the photon frequency and $a^\dagger a$ the harmonic oscillator ladder operators. While the second term $1/2\hbar\omega_d\sigma_z$ is the energy of the two-level system, σ_z being the pauli-z spin operator and ω_d the angular frequency of the dipole. The final term is $g(\sigma_+ a + a^\dagger\sigma_-)$ and is the coupling term which contains the coupling constant g. The factor g tells us at which rate our artificial two-level atom will absorb or emit photons from/to the resonator, and is also called the coupling strength, while $\sigma_\pm$ are the raising and lowering operators of our dipole . If g is larger than any decoherence rates in our system, then the photon and the dipole are said to strongly couple, and create a hybridization of light and matter. This means that if we want to use this phenomenon for transporting quantum information the field and dipole have to interact stronger and faster than the photons' rate of decay (or leaving the resonator), and than the electron's interaction with its environment. The dispersive regime [12] is defined as

$$g << \omega_r - \omega_d. \tag{2}$$

Thus we are in the dispersive regime when the coupling rate g is much smaller than the difference of the photon and dipole energy, which is the case when the photon frequency has a different frequency than the dipole resonance frequency. When the photon and dipole are out of resonance with each other, the interaction can modeled as a weak perturbation, yielding a coupling strength proportional to $\frac{g^2}{\omega_r - \omega_d}$. This gives rise to a dipole state dependent shift in the photon frequency ω_r, [13, 10]

$$\omega_{r'} = \omega_r \pm \frac{g^2}{\omega_r - \omega_d}. \tag{3}$$

This can thus be used to detect small capacitive changes in the dipole system. In our case, when charge reconfigurations alter the density of states in the InAs NW and thus cause a change in quantum capacitance, which we then can measure [12] .

2.2 High-frequency readout resonators

The resonators used in this thesis are modelled as superconducting microstrip $\lambda/2$ resonators. The resonators have a total inductance L and capacitance C depending the characteristic lenght **l** and geometry of our NbTiN microstrip. Where $\lambda/2$ denotes that the characteristic length of the resonator is one half of the wavelength at resonance frequency. Resulting in a resonator that either has voltage anti-nodes at $\mathbf{l} = 0$ and $\mathbf{l} = l$ if the resonator is open at $\mathbf{l} = 0$ and $\mathbf{l} = l$ **Fig.1 b**, or voltage nodes at $\mathbf{l} = 0$ and $\mathbf{l} = l$. The microstrip is comprised of infinitesimal portions of inductance pr. unit length L_l in series, and capacitance in shunt C_l as pictured in **Fig. 1a**. The inductance pr. unit lenght L_l consists of a classical geometric inductance contribution which stems from the magnetic field induced by current running in the line, as well as a kinetic inductance. The two contributions pr. length add up to a total contribution [12].

$$L_l = L_m + L_k \tag{4}$$

The kinetic inductance is a phenomenon that can be very pronounced in superconductors[1] due to the high velocity movement of electrons in systems with very low scattering times, due to the electrons own magnetic fields trying to slow them down upon accelerating in the resistance free environment. The capacitive element per length consists of a self-capacitive term C_s from the resonator's own windings, and a capacitance to everything else C_c, mainly between the resonator and the ground plane under the substrate upon which the microstrip is fabricated. As the two capacitance contributions are in parallel they sum up to a capacitance pr. unit length like the following [14]

$$C_l = C_s + C_p. \tag{5}$$

Assuming little losses for modelling purposes the resonance frequency and characteristic impedance of a LC circuit are given by

$$fr = \frac{1}{2\pi\sqrt{LC}} \ , \ Z_r = \sqrt{L/C} \tag{6}$$

. Where L and C are as aforementioned the total inductance and capacitance for a given length resonator [14]. Z_r is the characteristic impedance of our resonator, in our case simulated to be $1K\Omega$, in order to prevent microwaves from just entering and immediately leaving via the feedline. An important measure for our resonator is the quality factor Q . Q factors are equivalent to the dampening factors of a classical mechanical oscillator. The Q factor is a dimensionless quantity which describes the ratio of energy stored in the resonator to the energy dissipated pr. cycle by dampening [14].

[1] However also exists in normal conductors, but is just very small.

$$Q = \omega_0 \frac{Energy\ stored}{Power\ loss}. \tag{7}$$

If Q is high, it means that that the photon losses are low, and also that it takes more time for a photon to enter and exit the resonator. If Q is low, it means that the photon loss is high, and many photons enter and exit. The total Q_L [14] is called the loaded quality factor, and consists of a internal term and an external term

$$Q_L = (\frac{1}{Q_{int}} + \frac{1}{Q_{ext}})^{-1}. \tag{8}$$

The internal term is a measure of intrinsic loss in the resonator, for example dielectric losses to the substrate, and resistive losses due to defects of the NbTiN thin film. This being something that is in practicality determined by the quality of fabrication and size. The external losses come from radiative losses to the circuitry connected to the resonator, the feedline feeding it photons and in our case voltage controlled gates connected to the nanowire, and even to the surroundings. The internal quality factor Q_{int} for an open $\lambda/2$ resonator is defined as

$$Q_{int} = \omega_0 Z_r C = \frac{Z_r}{\omega_0 L}. \tag{9}$$

While the external quality factor Q_{ext} is dictated by the impedance miss match between the feedline and the resonator Z_{in} and Z_{out} between the resonator and load, and the capacitive coupling between feedline and resonator C_{in} and resonator and load C_{out}. The following expression shows this dependence and is derived in appendix A.

$$Q_{ext} = \frac{2C_{in}C_{out}}{\omega_0(Z_{out}C_{in} - Z_{in}C_{out})}. \tag{10}$$

The idea being that the impedance mismatch between the elements should act as mirrors, having Z_{in} and Z_{out} high enough to keeping the photons trapped, but Z_{in} exactly low enough to let some photons in to the resonator. Q_{ext} thus governs how well the photons enter and leave the resonator.
A final important factor for characterizing our resonators is the photon decay rate κ and a characteristic decay time T_κ are given by [5]

$$\kappa \approx \frac{fr}{Q_L}\ ,\ \ T_\kappa = 1/\kappa. \tag{11}$$

This information can be harvested by measuring transmission trough the feedline, where the power of the signal sent will be absorbed by the resonators at its resonance frequency. We can then obtain the

quality factors by fitting the S-parameter transmission amplitudes from the scattering matrix [14].

$$S_{ij} = \frac{V_i^-}{V_j^+} \ , \ S = \begin{pmatrix} S_{ij} & S_{ij} \\ S_{ij} & S_{ij} \end{pmatrix}, \ for\ i = \{1,2\}\ and\ j = \{1,2\} \tag{12}$$

Each element being the ratio of the reflected $(V_{i,j}{}^-)$ and incoming $(V_{i,j}{}^-)$ voltage wave, at either input or output while $V_k^+ = 0$ for $k \neq j$. The second index being the port delivering the input signal and the first index being the port measuring the signal. Thus the elements can either represent transmission(S_{12}, S_{21}) or reflection(S_{11}, S_{22}).

2.2.1 Fitting the resonances

The function we use to fit the transmission component S_{21} to extract the quality factors originates from rewriting the transmission coefficient S_{21} in therms of Q factors at the resonance peak which is expected to be lorenzian. Following equations are derived in Appendix B and C,

$$S_{21} = \frac{\frac{Q_L}{Q_{ext}}}{1 + (Q_L 2\frac{\Delta\omega}{\omega_0})}. \tag{13}$$

The expression utilizes the bandwidth of the resonance valley, which is directly linked to the loaded quality Q_L, and the insertion loss which is linked to the internal quality factor Q_{int}. In the combination of S_{21} and the insertion loss

$$IL = -10log\frac{(1 - \frac{Q_L}{Q_{int}})^2}{1 + (Q_L 2\frac{\Delta\omega}{\omega_0})^2}, \tag{14}$$

we can extract the external Q_{ext} factor

$$Q_{ext} = \frac{\omega_0}{\Delta\omega_{FWHM} \cdot 10^{\frac{-IL\omega_0}{20}}}. \tag{15}$$

The fitting function used throughout this thesis is a more advanced version of eq. 12,13 and 14 combined, which includes a couple of extra fitting parameters making up for asymmetries in the resonance peak. We can thus extract the internal quality factor, which gives us an overview of how well our resonators perform.

$$S_{21} = A(1+\alpha\frac{f - f_r}{f_r})(1-\frac{\frac{Q_L}{|Q_{ext}|}e^{i\theta}}{1 + 2iQ_L\frac{f-f_r}{f_r}})e^{i(\phi_v f + \phi_0)} \tag{16}$$

A is the transmission amplitude away from resonance and f_r is the resonance frequency. The Q factors are as previously defined. α is a fitting parameter that allows for small linear variations in

the resonance valley. $e^{-i\theta}$ is related to a the complex part of the external Q_{ext}, giving rise to a slight asymmetry in the resonance. ϕ_v and ϕ_0 account for the propagation delay to and from the load Z_L [15].

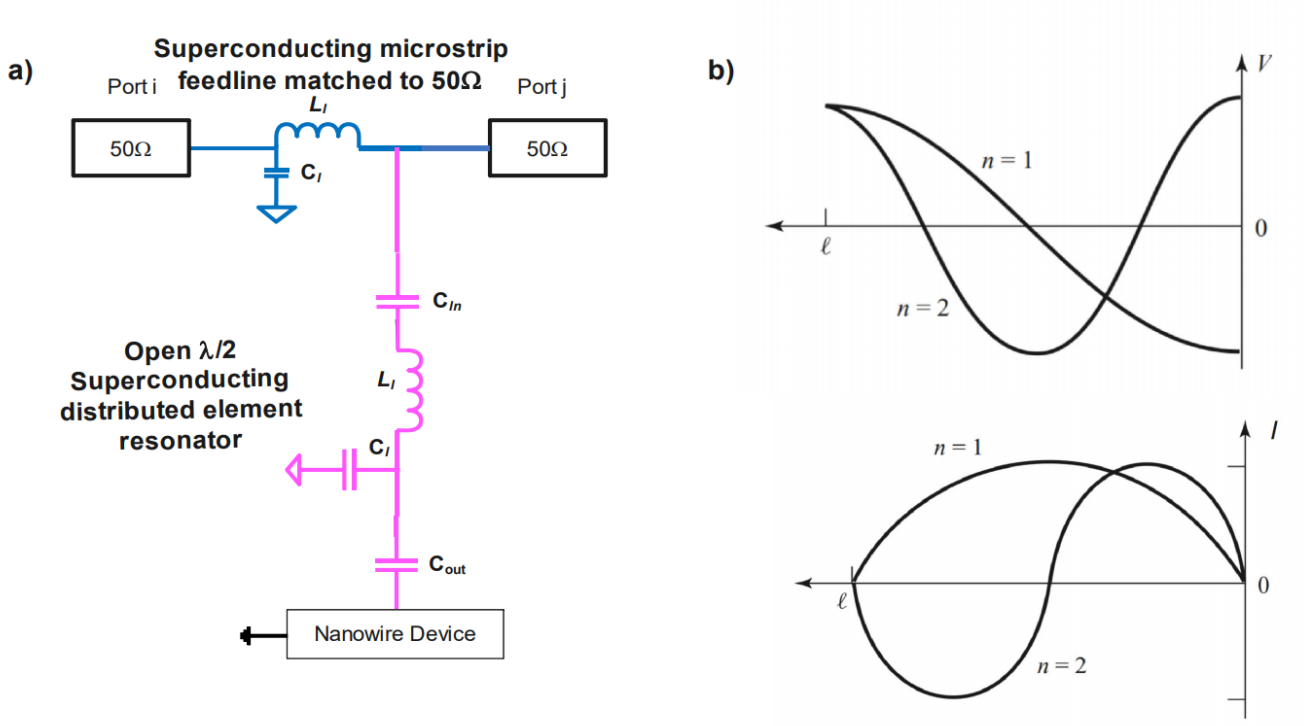

Figure 1: a) Schematic of the resonator device connected to the NWdevice. Blue circuit depicts the feedline modelled as a 50Ω matched distributed LC circuit with port i and j corresponding to the S matrix indicies . The pink circuit is the $\lambda/2$ distributed element LC resonator with C_l, L_l capacitive and inductive elements pr. unit length. C_c is the capactive coupling between feedline and resonator and C_{out} is the capacitive coupling to the nanowire device. **b)** Voltage and Current behavior in the $\lambda/2$ open resonator, with a length l, as we see current is zero at the nodes, while voltage is maximal. Meaning the electric field is largest at the nodes, which ultimately is what interacts with our nanowire device. Current and voltage mode images are adapted from [14].

2.3 Double quantum dots

In this section, we briefly introduce quantum dots (QDs), with a focus on double quantum dots, and what physical considerations go into the design effort, in order to lay the groundwork for coupling them to superconducting resonators. QDs are nanoscale objects, which can be either metallic, superconducting or semiconducting. What makes them unique is that they confine the electron's Fermi wave function in all three spatial directions. Hence they are sometimes referred to as 0D structures [16]. We will not delve deep into the theory of quantum dots, but several excellent reviews exist, most noticeably [17].

We model the NW device as a multi-gated field effect device with Hafnium Oxide as a dielectric, InAs as the substrate, five metallic gates [2] and metallic ohmic contacts to a source and drain reservoir on each side as in fig. 2a. We can apply a negative voltage to one of the gates in fig. 2a, to repel electrons, and a positive to attract them, thus creating a gate controlled quantum dot [16].
We measure the current I_{SD} from source to drain, as a function of the plunger gate voltages as seen in fig. 2a. I_{SD} shows periodic oscillations fig. 2b. as electrons tunnel into and out of each dot. This phenomenon is called Coloumb blockade (CB), which happens due to the electrons needing to overcome a Couloumb repulsion energy, which is determined by the DQDs self capacitance and and the number of electrons on each dot [17]. As electrons tunnel in and out of the dots due to changes in the plunger gate voltage, a small change in capacitance occurs between the gates and the semiconductor.

$$C_{diff} = \frac{dQ}{dVg} \tag{17}$$

Upon these small changes in capacitance, the frequency of the resonator shifts due to the change in the load impedance. This is commonly referred to as a dispersive shift. These shifts can then be measured, as electrons tunnel in and out of dots, thus enabling us to map out charge stability diagrams [18, 19].

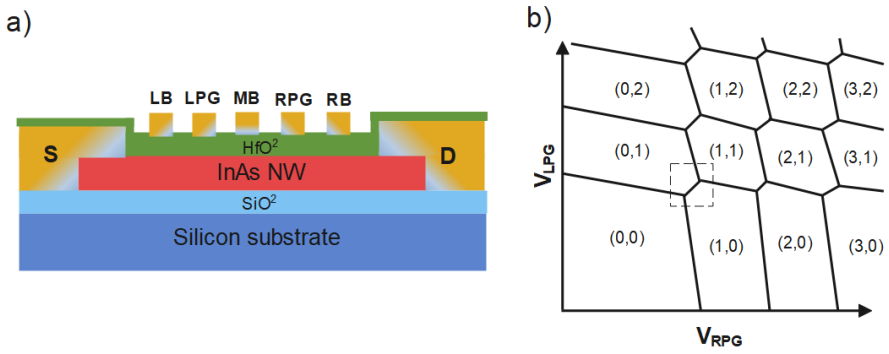

Figure 2: **a** Portrays the DQD structure of our NW device, LB is left barrier gate , LPG is left plunger gate, and MB is middle barrier gate ect.**b** Charge stability diagram of an ideal DQD system with LPG voltage along the y-axis, and RPG voltage along the x-axis. As we increase the voltages we add electrons to the dots as denoted (N_{RPG}, N_{LPG}), the box surrounds an area where one electron is delocalized among the two dots. Adapted from [17]

[2] In this thesis I refer to gate electrodes as gates, not to be confused with computational gate operations.

3 Experimental techniques

Here we go through the basic elements needed for conducting cryogenic low power experiments and how they were used. From the various high precision instruments, to the dilution refrigerator setup.

3.1 Cryogenic setup

The core component of most experiments performed at the 'Center for Quantum Devices' is the dilution refrigerator. Using a closed loop $^3He/^4He$ dilution cycle, mK temperatures can be reached [20]. These temperatures are crucial in the field of quantum transport to avoid the thermal smearing of quantum effects.

The dilution refrigerator used for the measurements in this thesis is an Oxford instruments Triton 400 cryogen free dilution refrigerator. This model is sectioned into six thermally insulated plates portrayed in fig. 3. The top plate (at 300 K) is where all the external wires enter. The pulse-tube plates, PT1 (at 55 K) and PT2 (at 4 K) are connected to the two stages of the pulse tube that is compressing and pumping helium into the system. PT2 is in direct connection with a heat exchanger which precools the returning ^3He, rendering it a plate with high cooling power, allowing for components that dissipate energy, like amplifiers. The still (700 mK) plate is thermally connected to the potstill where the dilute ^3He phase becomes vapour again with the help of three heat exchangers. It is followed by the 100mK plate, containing leads for incoming concentrated mixture and for outgoing dilute mixture. The mixing chamber(MC) is where the $^3He/^4He$ dilute phase and expansion occurs, being the plate with the lowest temperature; however it also has the lowest cooling power, of $\approx 1\mu W$ [20]. The MC plate in our fridge T7 is able to reach temperatures between 16-30 mK. The coldfinger (CF) is thermally anchored to the MC plate and is where we attach our sample puck that holds our experiment device in its printed circuit board (PCB).

Incoming from two breakout boxes, we have 96 DC lines going down, with 48 lines on each breakout box. The breakout box can open or ground each line with a switch. The DC lines are braided constantan looms thermally anchored onto each plate with a total resistance of 266 Ω (133 Ω For some lines). Located at the MC plate the DC lines enter 2 stages of low-frequency low-pass filters and 2 stages of high-frequency low-pass filters with a total resistance of $2.1K\Omega$($1.9K\Omega$ for some lines which have different filter models) before reaching the sample holder motherboard located inside the sample puck.

Furthermore, we have 22 Coaxial high frequency lines going in, equipped with different attenuators that have the job of reducing Johnson-Nyquist noise by thermalizing the electrons. The lines used in this thesis are coax 9 with a total attenuation of 55 dB, made of stainless steel until the last part

that is electrically connecting the MC to the CF which is made of flexible silver-plated copper. Tx and Rx are transmission and reflection ports, in our setup we have 2 pairs, called A and B. TxA (TxB) has an attenuation of 22dB (22dB) before reaching our decouplers that only send the reflected signal back up through RxA (RxB), adding an additional attenuation of -20db (-20dB). The Rx lines are our output lines equipped with DC blocks and amplifiers for the outgoing signal, RxA is equipped with a Weinreb +40dB amplifier, while RxB is equipped with a Low Noise Factory +25dB amplifier.

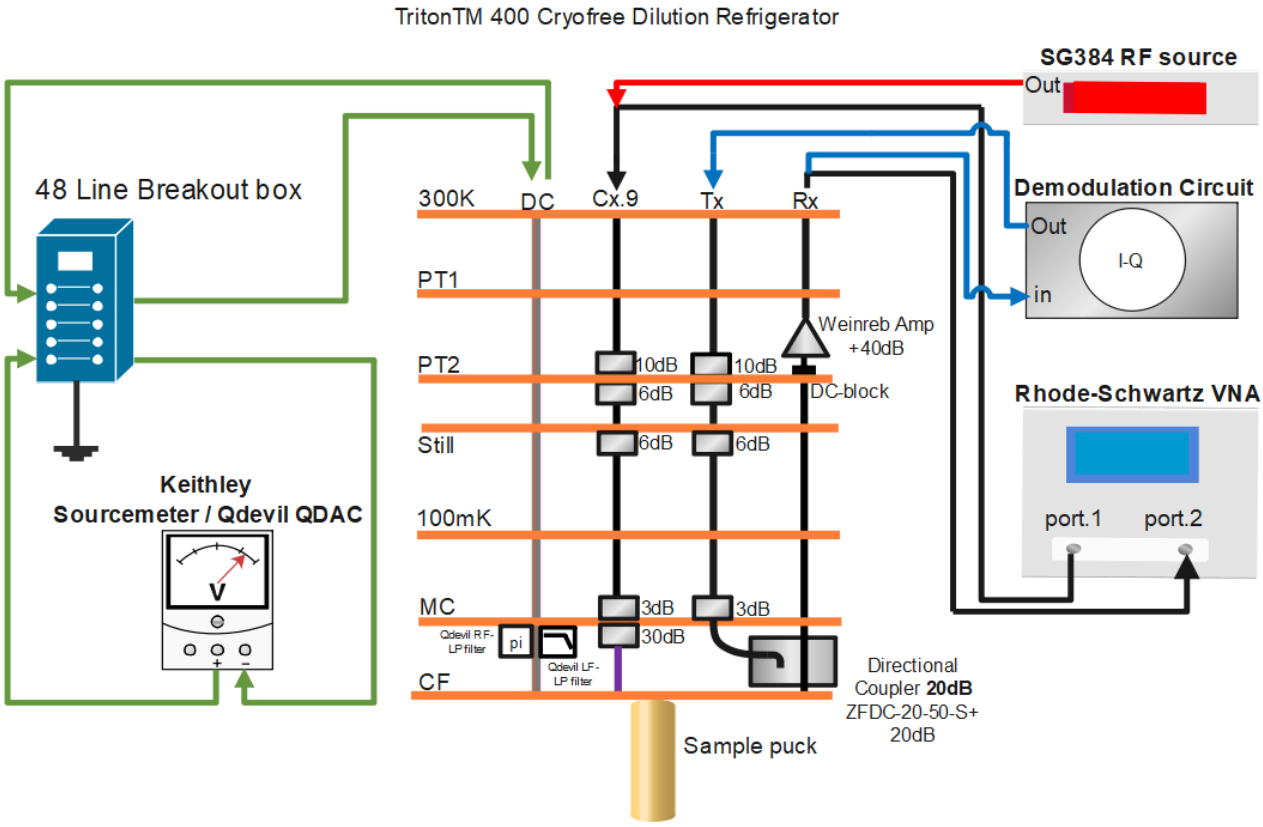

Figure 3: Schematic of the full experimental setup. Left side depicts the breakout box connecting to various DC sources. The middle contains the dilution refrigerator sectioned into various stages of temperature, including the attenuation and amplification of the various important lines, all leading to the sample puck connected to the cold finger that has a temperature of 17-30 mK. The right side contains the high frequency instruments connecting to their respective coaxial cables. Note that the VNA is not used simultaneously with the demodulation circuit.

3.1.1 Low-frequency measurements

Low frequency measurements are done using the DC lines, enabling us to control various parameters on our devices. The two main instruments used for performing these measurements and manipulations are the Keithley source meter and the QDevil QDAC. The Keithley 2614B is a high precision SMU, with the ability to output (Max$\pm$100 V, Min100 nV) and measure (Max.$\pm$10 A, Min$\pm$100 fA) with the same channel. The Keithley has 2 ports, making it an ideal tool for analyzing gate leakage and I/V characteristics. The QDevil QDAC (Digital to analog converter) is a 24 channel voltage source, with the ability to output $\pm$10 V often used in combination with a DMM to measure current. Ideal for multi-gate devices, which need many different voltage parameter settings.

3.1.2 High-frequency measurements

The ZNB Vector network analyzer (VNA) can be described as a mix between a signal generator and a spectrum analyzer. It is used for extracting both the real and complex components of the transmission and reflection coefficients of the scattering matrix as discussed in section 2.2. It does so by outputting an AC voltage with a user set power in dBm, for every frequency in a user defined interval. Upon each measured signal it multiplies it with a reference signal. Storing the amplitude in dB and phase difference between the reference in-phase and quadrature signal. We use this tool for identifying resonator resonance frequencies by measuring transmission S_{12} or S_{21} for different input powers powers.

We also use a RF source generator SG384 that can output a sine wave with a frequency from DC-4GHz with powers spanning -10 dBm to +13 dBm. In this thesis we use this tool to probe different resonance frequencies revealed by the VNA, in order to see how they respond. The final technique we use is Rf reflectometry. By using a demodulation circuit and performing homodyne detection. This technique is useful for high-frequency readout of charge configurations. Due to fast changes in the impedance of the sensor dot, which the resonator is connected to; the reflected signal changes which we measure after demodulation. We do this by the use of port Tx and Rx, and a demodulation circuit. The demodulation circuit works by having a probe signal which interacts with the DUT (Device under test), and a reference signal locked to the probe frequency. After the probe signal interacts with the DUT, the referance signal and probe signal get mixed by a microwave diode mixer. The nonlinearity of the mixer creates a multitude of frequency products which we can remove with a low pass filter, only leaving a 'demodulated' DC voltage. Thus by merely tuning the gates of a DQD device a change in quantum capacitance can be detected with the use of RF reflectometry. We can thus extract discrete charge information without having to actually apply a voltage over the source and drain of a device. Rendering it a fast, precise, and, non-invasive measurement technique.

4 Devices and fabrication

In the following chapter we outline how the various on-chip resonators, off-chip resonators and NW devices were fabricated, including design specifics and considerations. On-chip meaning that the resonator is fabricated on the same substrate as the NW device thus being on chip. Off-chip being a separately fabricated resonator on its own chip. All resonators and on chip resonator-NW devices were fabricated in house at Center for quantum devices. Some other double quantum dot devices were used to test the bonded quality factors with the off-chip resonators before we finished our first batch of NW devices, namely a silicon CEA Leti[3], foundry made quantum transistor device which I will not discuss further. The in house fabrication of resonators and NW devices were done in four batches on a highly resistive (5 kΩ/cm) silicon substrate. The fabrication process was done in the following steps[4].

- Bondpads, outer gates and markers are done with electron beam lithography using a elionix 125 kV e-beam system. Metalization is done with Au evaporation in an AJA electron beam evaporator.
- Resonator arrays are done with electron beam lithography, followed by plasma sputtering of NbTiN film with an AJA electron beam evaporator.
- NWs are placed using a micromanipulator and are SEM imaged for post placement of source and drain ohmics and gate design.
- The nanowire covered in a layer of HfO_2, followed by RF milling some of the HfO_2 in order to deposit ohmics on each side of the nanowire.
- Topgates are also done with e-beam lithography, and are metalized with evaporation of either Au og Al gates in the AJA.

4.1 Superconducting resonator arrays

The NbTiN resonators are fabricated in a multiple of three resonators pr. chip[5]. Thus each 'on-chip' and 'off-chip' resonator device consists of three resonators coupled to a two port feedline surrounded by a grounding plane. The resonators are designed in a square spiral design to increase the length and simultaneously minimize the footprint. Each of the three spiral resonators per feedline has two

[3]The French Alternative Energies and Atomic Energy Commission - Laboratoire d'électronique des technologies del'information (CEA-Leti), a research foundry providing us with silicon field effect transistor-based quantum dot devices as part of the EU Horizon 2020 MOSQUITO project.

[4]lithography, deposition and milling steps were done by Fabio Ansaloni and Bertram Brovang, while NW placement was done by me (Lazar Lakic).

[5]This was simply done in order to increase yield and to test different resonance frequencies at once.

coupling pads. One pad is either placed close to the feedline in order to increase capacitive coupling with the feedline, or inside the resonator to obtain inductive coupling instead of capacitive. The other pad is to be connected with either a fabricated lead to the device ('On-chip'), or a wirebond ('off-chip'). Multiple variations of spirals and pads were made in order to to obtain better coupling properties. The device was initially designed by Pasquale Scarlino and simulated by Niels Søe Loft using python addon - QuTIP quantum tool box and HFSS at NBI - Qdev. Simulations were done using Aluminium instead of NbTiN as it was easier to simulate without incorporating kinetic inductance . However this does not present a problem as it still provided estimates of resonances, although to high. As the real resonance frequencies would become lower due to the high inductance. The resonance frequencies aimed for span from hundreds of MHz to the early GHz regimes which is ideal for RF reflectometry experiments in semiconductor devices [19, 18]. Coupling leads, wirebond lengths and wirebond capacitances were not included in the simulations also lowering resonance. Additionally, various spiral and pad designs were made. Experimenting with both resonator length, connection pad placement and pad-to-feedline coastline length in order to increase capacitive coupling to the feedline. Details of capacitive and inductive coupling between resonator and feedline can be seen in fig.11.

4.1.1 Designs

- **The Tucuxi style resonator arrays seen in fig. 4b and d** : consist of a feedline and three resonators with 6, 4 and 2 turns. Common for all Tucuxi designs are that one pad is located in the spiral, and the other outside of the spiral. The variations all play with placement of the outer pad and or the pad to feedline coastline length. The individual resonators on each array are dubbed A, B and C from left to right as they are facing in fig. 4b.

  – NbTiN film Resonators

  – 4450μm feedline length.

  – 15μm spacing between resonator turns.

  – High fabrication yield due to the big features of the resonator.

  – Nose and big pad design lengths: A=3mm , B=6mm, C=9mm

  – Inductively coupled Tucuxi design as seen in fig. 4d. lengths: A=4mm , B=8mm, C=12mm

- **The Kawili'Kai resonator array design seen in fig. 4c.**: consists of a feedline and four resonators shaped like a Fermats spiral, meaning that both pads are located outside the spiral, while the spiral funnels in and then out. This design is an attempt to increase capacitive coupling to the

feedline, and leave out any inductive coupling. Also making it possible to do an easy on chip bonding to wire, avoiding having to bond inside a resonator.

- NbTiN film Resonators
- 4450μm feedline length.
- 15μm spacing between resonator turns.
- High fabrication yield due to the big features of the resonator
- Resonators lengths: A=2.5mm , B=5mm ,C=7.5mm, D=10mm

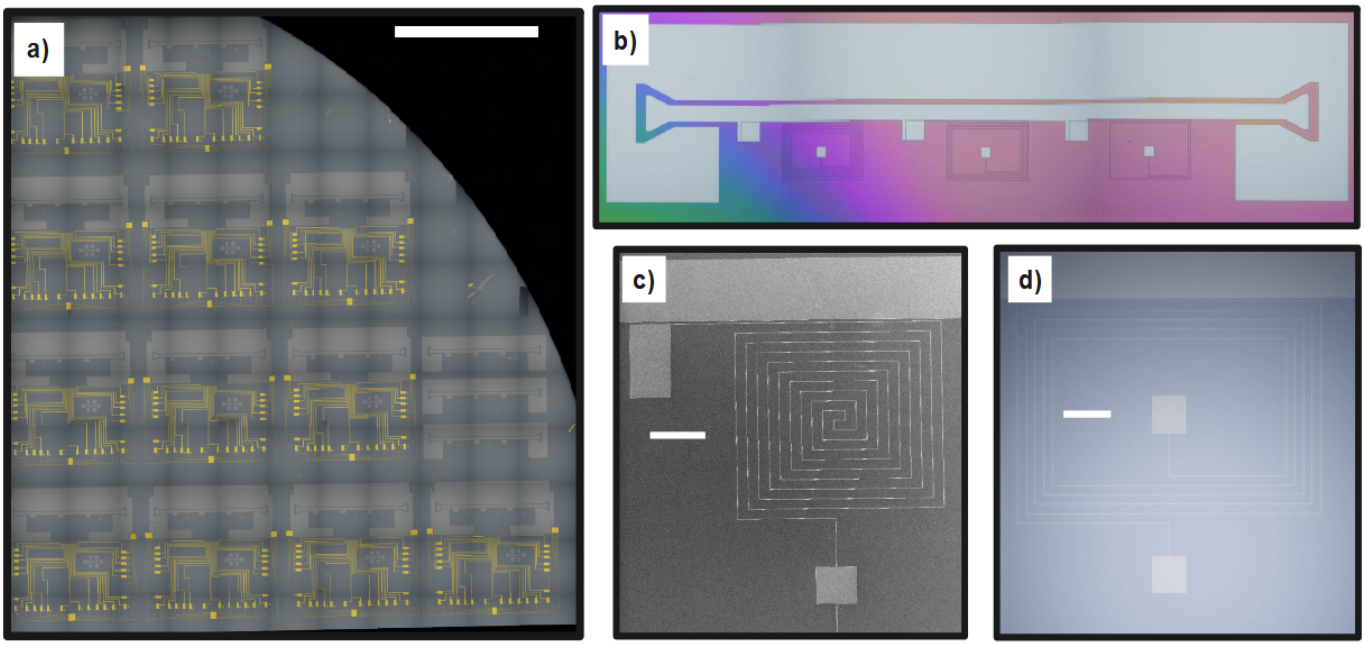

Figure 4: a) Optical photo of a quarter silicon wafer with 12 'on-chip' resonator arrays and 36 nanowire devices (three pr. device). Including three 'off-chip' resonator arrays. White scale bar is 5.3 mm. **b)** Optical photo of an 'off chip' Tucuxi resonator array with a 'big nose' design. Feedline is 4.45 mm long. The iridescent colour stems from light hitting the PMMA resist protecting the resonator. **c)** SEM photo of Kawili'kai (Fermats spiral) resonator, white scale bar is 100 μm, the white kinks along the resonator spiral are due to a fabrication error. **d)** Optical photo of an inductively coupled Tucuxi design, the white scalebar is 100 μm.

4.2 Nanowire Devices

The NW devices were made in multiple batches on quarter pieces of a 4"inch silicon wafer. Each quarter containing about 10-13 chips at a time. Each sample chip has a resonator array and three NWs - each to be connected to one of the three resonators. Each NW has a source and drain ohmic on each

end, and either 5 side gates, 5 bottom gates or 5 top gates. The semiconducting InAs NWs were grown in-house, with a length of 3-4.5 μm.

- **Jamaica and Aruba batch**: Were done as a process test. Including both top gate, bottom gate, and side gate designs. Gates were done in Au, with a gate width of 130-150 nm, gate spacing of 80-100 nm, and ohmic to ohmic spacing of 200-250 nm. Post fabrication looked good, with few visible deformities like cracks in the gates at areas that were not properly exposed. About half the wires were conducting, however the side and top gates that worked were not strong enough to pinch off the current in the nanowire during transport tests. Many bottom gates did not peel off properly during lift off or got scratched heavily during micro manipulation.

- **Bahamas batch**: Was initially intended to contain half Al bottom gates, and half Al overlapping top gates. The Al bottom gates did not survive resist lift off in dioxilane, and the entire 11 devices, were remade into Al topgates after NW deposition. Fabrication yield was however very low. 4 devices suffered a misalignment problem, with gate offshots of 50-200 nm, this could either be attributed to have happened during resist spinning before the lithography step causing some of the NWs to move a bit, or mistakes made during CAD design[6]. The rest of the gates had problems climbing the NWs, causing shallow Al deposition and inter-gate current leakage. Thus Bahamas had a low fabrication yield.

- **Tortuga Batch**: Was a second attempt to do overlapping Al gates, with the same design as the Bahamas batch. However something went wrong, and the entire 13 devices, nanowires and gates included were blown up. This was identified upon the final SEM, after gate lift off. Assumed to have been caused by an electro static discharge (ESD) collectively blowing up the devices.

[6] Like accidentally using wrong NW SEM photos.

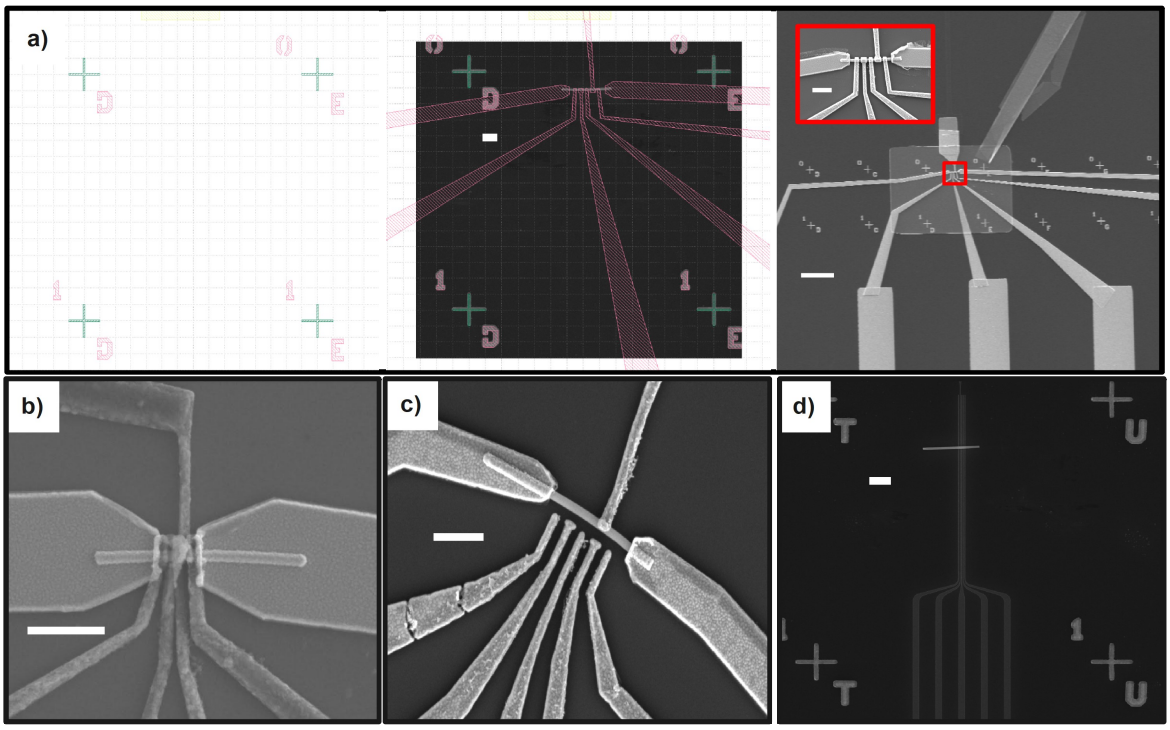

Figure 5: a) Bondpads, outer gates and markers are made in cad then fabricated. Nanowire is placed and a SEM photo is taken. Then we insert the SEM photo and design the source and drain ohmics and gates, followed by fabrication in 2 rounds. Scale bar on second picture is 1 μm, third picture 10 μm, inset in third picture 1 μm. **b)** Overlapping top gate design, notice the grainy aluminum and the shallow spots before the gates meet. **c)** Side gate design with a few cracks in the Au gold leads. **d)** Bottom gate design after NW placement, and before ohmic deposition.

4.3 Micromanipulator

Nanowires are placed using a micro-manipulator. The micro-manipulator is essentially a high precision 'tong' that by Van der Vaals forces and a human controller can move and place micron sized objects. The micro- manipulator is realized by combining an optical microscope, a movable stage, and an "Eppendorf TransferMan"[7] controllable arm equipped with a 0.1 μm tip-diameter electrical probe needle. Picking up the NWs from growth substrate and placing them onto device. A total of 108 NWs were placed in this project.

[7]Which original intent is manipulating cells and other biologic matter

5 Experiments and results

5.1 Device characterization

5.1.1 Nanowires

Before cooling down a device, the ohmics, feedline, and gates are wirebonded to the respective high or low frequency pads of a QDevil 'Q126' daughterboard seen in **fig.7 a**. The green pads are DC lines, red pads AC lines, orange pads are bias tee lines with the option to be both AC or DC lines. The daughterboard is then contacted onto a interposer with fuzzbuttons residing on a motherboard, located inside of the sample puck. The puck contains all the electrical lines going to the motherboard which are routed out by nano-D (for DC) and SMP (for AC signals) connectors.

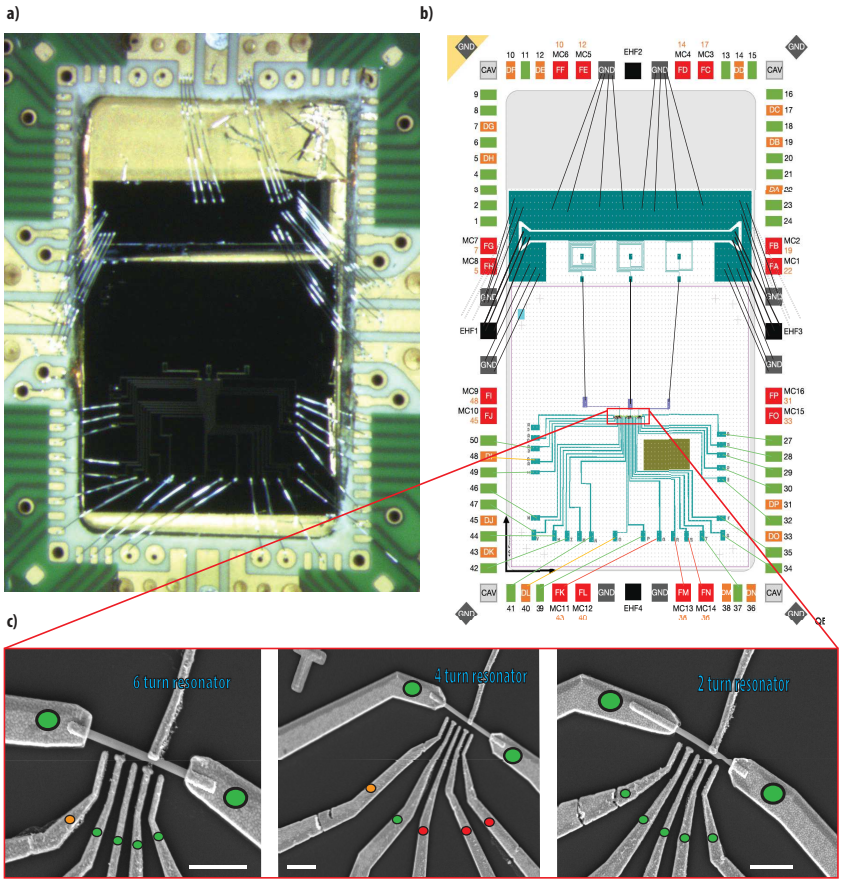

Figure 6: Overview of a 'two-chip' device and its electrical connections. ***a***) Optical photo of an 'off-chip' resonator (Top black rectangle) connected to a side gated NW device (black square). Both Located in a daugtherboard cavity and bonded to the daugtherboard. Wirebonds connecting resonators and NW devices were added post picture. ***b***) Wire bonding schematic for the 'two-chip' device in a). The coloured pads correspond to were we have various DC and AC connections on the daugtherboard. Green is DC lines, orange is bias tee lines that can be either DC or AC, red are AC line. GND is ground, and EHF1 are connections to high-frequency SMP connectors. ***c***) SEM photos of NWs A to C from left to right in the red region of b), The different colour circles indicate what the various gates and ohmics are connected to, corresponding to the colours in b). Scale bar is 1 μm.

The devices are then cooled to base temperature which is around 16-30 mK. Initially after cooldown a series of tests are performed in order to characterize the devices and confirm their functionality. Transport tests are done to be sure that the wires are conducting, and gates don't leak or are broken which can be seen in **fig. 7**. The nanowires are tested by grounding all gates and the drain on the breakout box and sweeping the source electrode with a Keithley sourcemeter. If no current is running from source to drain, the nanowire is not conducting like nanowire C in **fig. 7a**. We suspect the NWs were damaged by an electro-static discharge[8]. Unfortunately, fewer than half of our nanowires were conducting. The reasons for this are unknown and if the failure mode proceeds, post-measurement SEMs should be taken to confirm or rule out ESD damage.

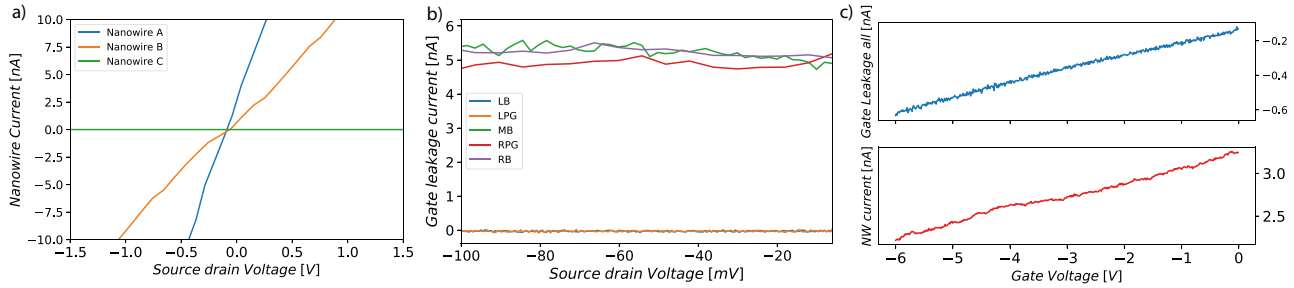

Figure 7: Nanowire characteristics of a sidegated NW device **a)** Conduction tests. Nanowire A conducts no current, while B and C conduct. **b)** Gate leakage tests of the 5 gates, showing no leakage for 'LB' and 'LPG', while the rest leak a current in the nA range for small gate voltages. **c)** Pinch off test by applying one gatevoltage to all gates. Showing no pinch off for gate voltages down to -6V

Leakage tests of individual gates are done by sweeping each gate with a Keithley or the QDac. If a current is flowing from a gate to ground, there may be a leakage, since a gate electrode should in principle be an open circuit. In case of leakage, all other connections are floated one by one in order to locate where the leakage flows to. Finally, to test whether the gates can pinch, all side gates are swept from 0 to -10V simultaneously, stopped if current starts rising fast. While a constant bias of 1mV is set on 'S' and 'D'. This is done to see at what voltage the current flowing from source to drain is stopped due to the electric fields from the gates. This current-stopping voltage is in device jargon called pinch-off. Sometimes pinch off does not occur before a high voltage on the side gates is reached - causing power dissipation in the order of mW, enough to start warming up the fridge. If the gates cannot pinch, this may indicate that the gates have a too low capacitive coupling with the nanowires, meaning that they are too small, too far away or in case of overlapping gates, that the oxide is too thick. If proper pinch-off is achieved, one can start to tune the gates into a double or single well potential in order to create quantum dots by adjusting gate voltages individually.

[8]Caused by ungrounded interaction between device and scientist

Nine out of 23 nanowire devices were fit for characterization, of which two were sidegated, three top gated with Au gates, one bottom gated, and three top gated with Al top gates. That means that a total of 27 NWs were two-terminal tested, of which 10 NWs were conducting. Hence a little more than 1/3 survived, all which had a ballpark resistance of 10-30 $K\Omega$. Out the 50 gates of the 10 working NW gates, only 27 did not leak. The Au gates did not have nearly as much leakage problems as the Al gates. Out of these 27 gates only 4 would pinch off current through the nanowire; this was observed on a topgated device, where the plunger gate connected to a resonator did however not work. A single dot was however tuned in this device, but deemed too big and unacceptably noisy, and the device was unloaded from the fridge to make room for new devices before meaningful data was acquired. All of these observations indicate a low yield, that can be attributed to several circumstances. The success with aluminium top and bottom gates was low, due to shallow deposition, and inability to climb the nanowire properly, and the few devices that were optically deemed fit for testing had severe gate leakage problems. Bottom gates were notoriously hard due to difficult lift-offs and micromanipulator accidents, so that only one bottom gate device made it to testing, where the NWs did not conduct. To combat the failure of our devices, we have initiated a final wafer, which systematically increases the gate spacing to find the optimal spacing using Au top gates. The NWs were fabricated in batches of many, as mentioned in section 4.2, to reduce fabrication time. However, we now suspect that doing it this way could leave room for critical errors. Instead of batches of 11-13 devices, 4-6 would maybe be better, to avoid a single accident destroying all fabrication progress on a batch (such as the Tortuga quarter-wafer as described in section 4.2). A better Al gate deposition could maybe also have been achieved if that process was tested over a couple of runs, instead of all at once. Another way to achieve better bottom gate yield would be to create many more bottom gates per chip instead of the three that we did, such that we have more room for error, and can choose the best NW depositions and bottom gates before wirebonding.

5.1.2 Resonator testing

Upon initial cooldown, we measured the transmission S_{21} amplitude as a function of frequency and temperature, aswell as the transmission S_{21} amplitude as a function of perpendicular and parallel magnetic sweeps and frequency. This was done to characterize the superconducting properties of the resonators and their feedline. The resonator is connected via coax 9 (in) and RxA (out), such that we can obtain the transmission magnitude along a frequency trace, taking a frequency trace every 10 minutes. **Fig. 8a.** below shows that we have no transmission from 9 K to 7.4 K, until suddenly the feedline turns superconducting allowing transmission, which matches the NbTiN film's critical temperature [21]. The resonators starts showing resonance at 6 K, becoming stable at 1 K and below,

additionally showing a not understood feature towards 1 K. When mK temperatures were reached we took a parallel[9] magnetic sweep and a perpendicular[10] magnetic field sweep. We observed that a parallel magnetic field does not break the superconductivity up till 3 T, which matches previous findings, and is attributed to the thin film resonator features not being able to sustain supercurrent vortices, thus not disrupting the superconductivity and thereby increasing dissipation [8]. However for a perpendicular field, the resonances start disappearing at 0.2 T-0.3 T due to supercurrent vorticies NbTiN [8].

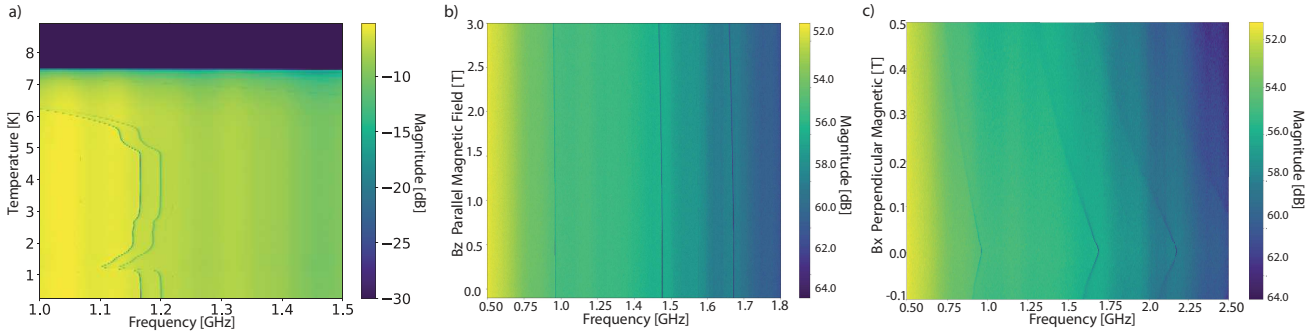

Figure 8: Temperature and Magnetic field characteristics of a NbTiN resonator. **a)** Measurements of S_{21} transmission magnitude on the VNA as a function of temperature and frequency. The measurement has a total line attenuation of 25dB. **b)** S21 magnitude measured as a function of parallel (w.r.t the device chip) magnetic field and frequency. **c** The same as **b)** just with a field perpendicular w.r.t the the device chip.

The resonances (f_r) of the resonators are measured with a VNA by taking a frequency trace. A -30 dBm signal trace is measured from 0 to 3 GHz. The signal travels from VNA port 2 through coax 9, into the feedline and out through RxA, with a total attenuation of 25 dB before it arrives back to the VNA at 'port 1'. As three resonators reside on each chip (in order to be able to address more than one device) it can be hard to differentiate between them. If they were perfect $\lambda/2$ resonators we would assume that the lowest frequency is the longest resonator, and the harmonics would then be multiples of that frequency. This however, is a bit unclear in our case, as we have large capacitive pads at the ends and galvanic connections between NW device and resonator that alter the effective lengths.

To get a better overview of what resonance belongs to which resonator, we came up with the idea of using a wave generator to apply a high power (13 dBm) sine wave with a frequency matching what we estimate is the fundamental mode of a particular resonator to the Tx coax line (not connected to the device) [11], while simultaneously measuring a VNA transmission trace via coax9 (port 1 of resonator) and Rx (port 2 of resonator). Since Tx is coupled with a directional coupler to Rx, we keep the output

[9] z-axis of device
[10] x-axis of device
[11] See Fig. 3

open to achieve full reflection. Thus we hope to see positive interference between the sent signal and the belonging resonance modes of the individual resonators. The result is described in fig. 9., where the red, gold, and green curves are measured with this technique. The blue is an ordinary transmission trace as described in the beginning of this section. Looking at the red trace in fig. 9., the signal applied at the estimated frequency lights up its corresponding resonance and reveals a possibly overseen resonance, at a lower frequency than the 671MHz resonance. It is reported that coupling to the fundamental modes is weak for similar super conducting resonators made of NbTiN films [22], and therefore this may well be a previously undetectable fundamental mode that is being lit up. The green trace, additionally, shows a response at 969 MHz and 1.90 GHz which roughly is in the ballpark of being multiples of each other. Finally, the gold trace for the 671MHz resonance barely lights anything up except for some of the higher resonances, and maybe is not a resonance at all. All three curves however show un-distorted resonances at frequencies we did not expect. This could be explained by the feedline being slightly mismatched, causing ringing that makes the harmonics of the sent frequency light up the other resonances, in the case that the resonators are so unfortunately designed that they all have fundamental modes that correspond to harmonics of each other. This was however not investigated further. By applying this technique carefully we could maybe identify the resonances prior to using them with the NW devices. Another compromise, in the initial stages of the project, could be to not to have multiple resonators on each feedline.

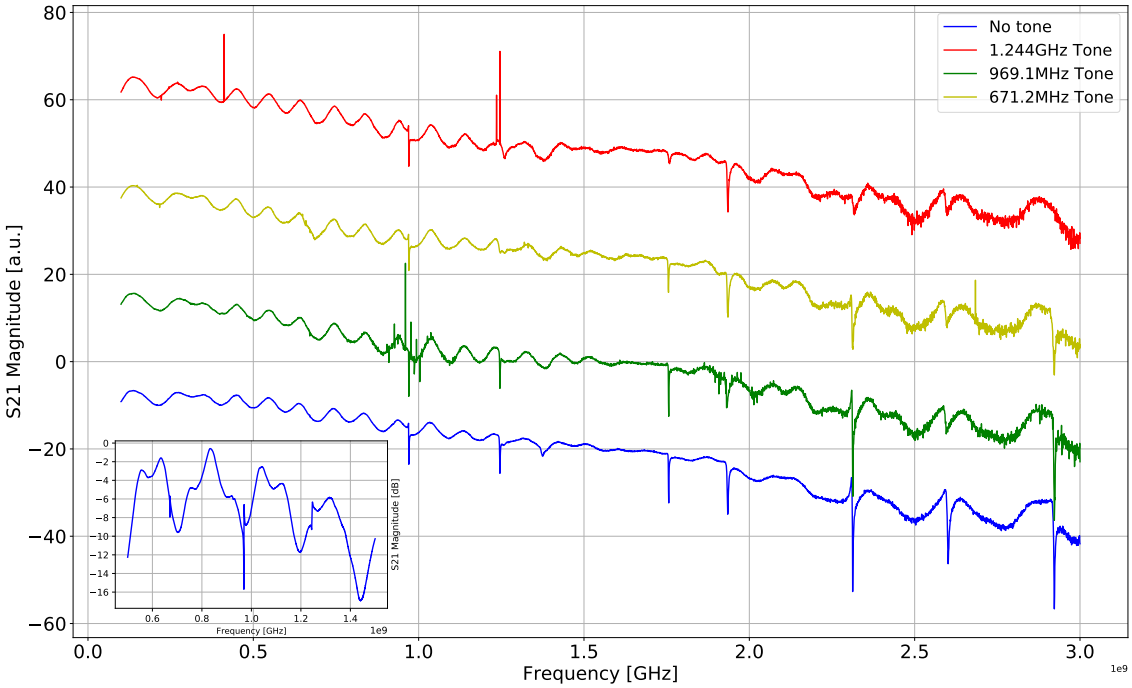

Figure 9: Transmission traces with an additional tone applied.Y-axis portrays A.U. of S_{21} amplitude as the red, green and yellow traces have intentionally offset. Blue trace has no tone applied, while red, yellow, and green have a high frequency tone corresponding to a suspected resonance applied by a Signal generator, with a power of 13 dBm. The inset is a zoom in containing the three first resonances of the blue trace from 300MHz to 1.4GHz on the x-axis with the S21 magnitude on the y-axis.

To fit the resonances and extract the Q values, we acquire the power dependence as seen in fig. 10a. Then taking vertical cuts and fitting the same resonance for multiple powers as seen in fig. 10b. Thus we achieve internal and external quality factors which can be used to derive the loaded quality factor. We implement Eq. (11) in a python using a script[12] written and adapted to our data acquisition software QCoDeS. We fit the S_{21} magnitude which fits to the loaded and internal Q factors to extract the external Q_{ext}. For every fit it does at increasing power, the software optimizes fitting parameter estimates. The code can both return the loaded, external and internal Q_{int}. Comparing fig. 10a and fig. 10b we see that the external Q_{ext} factor is unchanged with an increase in power, while the internal Q_{int} starts rising as the resonance decreases due to increased power. Thus we choose to determine the Q factors on background of fits done in the low power regime before the resonance shifts downwards.

[12]The script was written and kindly provided to us by Dr. David van Zanten.

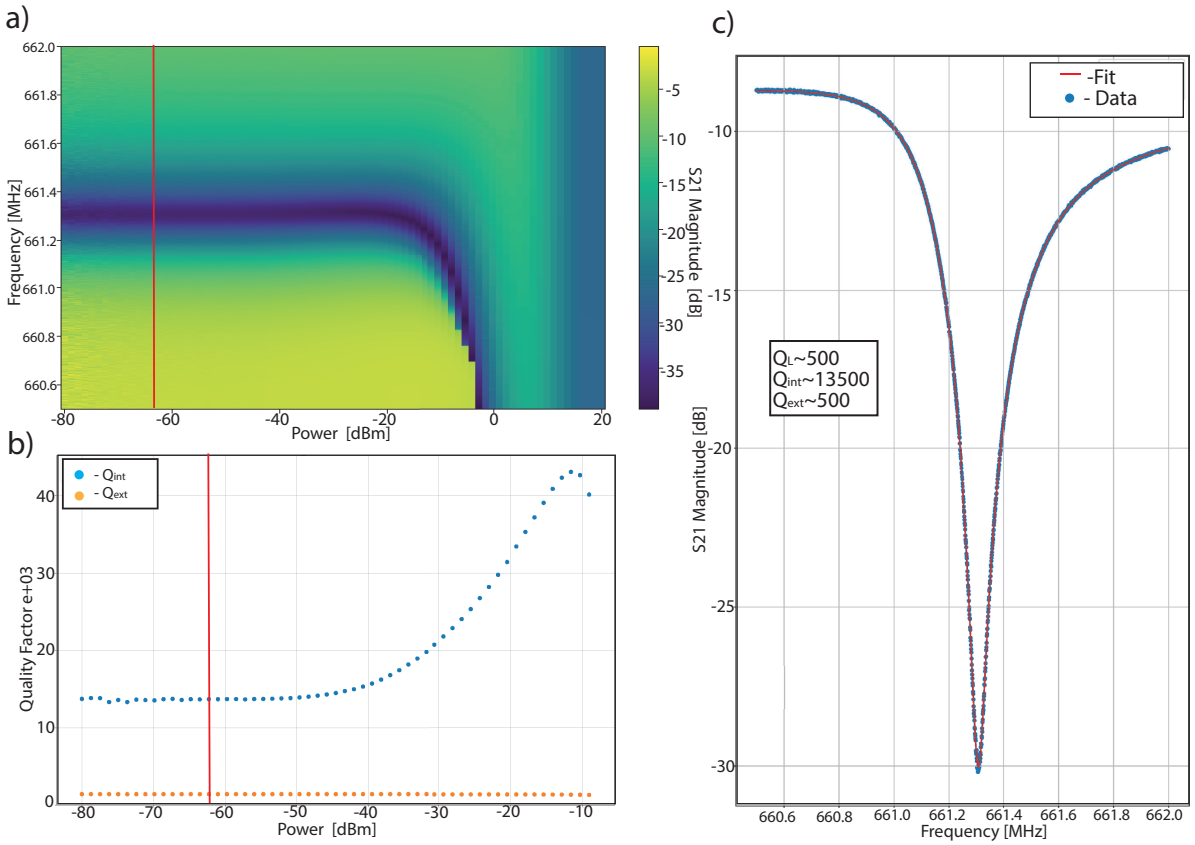

Figure 10: Resonator fitting. **a)** S21 magnitude as a function of power and frequency, red line corresponds to the trace in figure c). **b)** Quality factors acquired by fitting, each dot corresponds to a Q factor output by a vertical fit in a) **c)** The vertical cut from a) with the fit from eq.(11) applied.

We tested several designs and configurations, namely two 'off-chip' Tucuxi designs, one with a big feedline pad fig. 11a, and one with the same pad just with an added nose peg to increase capacitive coupling from the feedline fig. 11c. Furthermore we tested an 'on-chip' fermats spiral design wirebonded to a bias tee on one end and the NW device on the end (the same device was also tested unbonded fig. 11d) Finally we tested an 'off-chip' inside out Tucuxi (fig. 11b) design wirebonded to a bias tee acting as a simple lowpass filter and to the CEA Leti device (briefly introduced in section 4) this resonator was also tested unbonded.

Their Q values were extracted by averaging the multiple low power fit points for each resonance as shown in fig. 12b. Our goal was to investigate which configurations yielded the highest loaded and external Q factors. In fig. 12a,b and c, we observe that the loaded Q_Ls range from a few hundred to $1.4{\cdot}10^4$. Starting of by looking at the unbonded 'off-chip' resonators from fig. 11a. we notice that their Q_L values follow each other somewhat consistently; this was expected due to them being almost identical, except for the extra few μm of coupling coastline length between the feedline and resonator

for the nose design in fig. 11c. By comparing the external Q_{ext} in fig. 12g for the resonators in fig. 11a and c, we observe a slightly higher Q_{ext} for the nose design (fig.11c) than the design without the nose from fig 11a. Concluding that increased capacitive coupling to the feedline increases the loaded Q_L [14], which gives us an incentive to further pursue a design with a longer coupling coastline.

As for the loaded Q_Ls in fig. 12c we see a clear difference between the bonded and unbonded resonators from fig. 11b. The loaded quality factor being in the range of 10^2 to early 10^3 for the bonded one, where as the unbonded goes from $3.8 \cdot 10^3$ to $1.38 \cdot 10^4$. This turns our attention to the external Q_{ext} in fig 12i which also shows extremely low values for the bonded resonator, indicating that the bonding is enabling photon losses, whereas the unbonded resonator has external Q_{ext}s from $8 \cdot 10^3$ to $3.2 \cdot 10^4$ (we do not count the 0 outlier for the unbonded resonator).

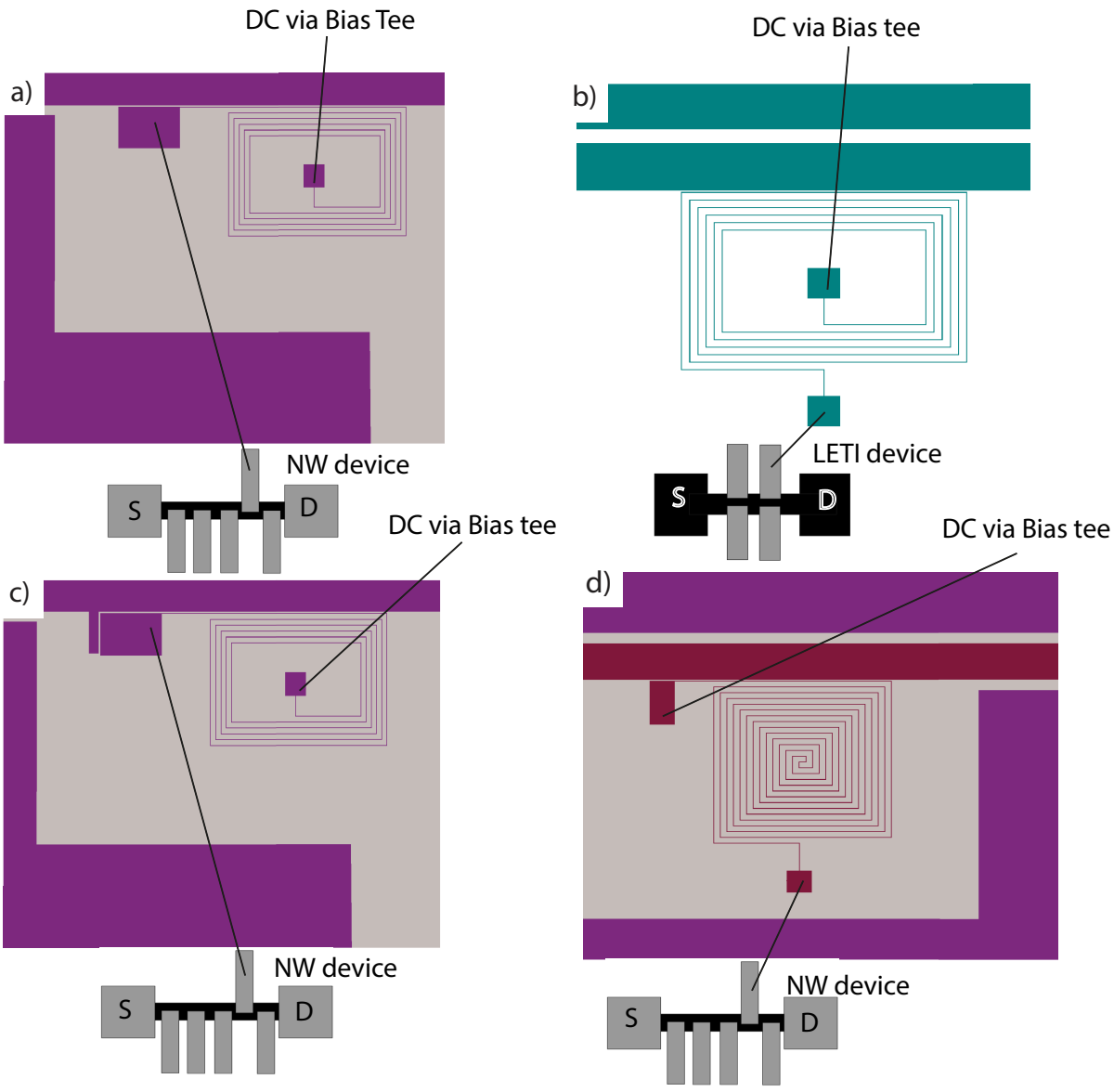

Figure 11: CAD design images of the resonators under investigation. Black lines indicate wirebonds. **a)** Tucuxi Big pad design. When bonded to a NW, a bias tee gets wirebonded to the inner pad of the resonator, while the feedline coupling pad gets bonded to a plunger gate of the NW device.**b)** The inductively coupled Tucuxi design, when coupling to a device, the inner capacitor pad gets wirebonded to a bias tee, and the outer to a plunger gate of the device under investigation. **c)** Tucuxi Nose design, coupled the same way as in a) **d)** Fermat spiral coupled the same way as in a).

Fig. 12b showcases the loaded Q factors of an 'on-chip' fermats spiral resonator in both bonded and unbonded state. Bonded means that the resonator is wirebonded from a bias tee to the feedline coupling pad of the resonator, and from the end node pad routed with an on chip nanostrip down to a pad in front of the InAs NW, where it then is wirebonded to connect with the right plunger gate as

seen in fig 2a. In this case, we again see that that the unbonded version has higher loaded Q_L factors than the bonded ones as expected. The unbonded Q_L factors are lower than all three off chip versions ranging from a few hundred to $9.5 \cdot 10^3$. Furthermore the bonded Q_L factors seem to be higher than for the bonded inside out Tucuxi at least for the frequencies ranging from 600 MHz to 1.1 GHz. The external Q_{ext} factors for the fermat spiral resonators (fig. 11d) range from a few hundred to $1.3 \cdot 10^4$ while most lie in the $\approx 6 - 8 \cdot 10^3$ range. While the bonded Q_{ext} lie steadily in the range $\approx 1 - 4 \cdot 10^3$ i.e. slightly higher than for the bonded 'off-chip' resonator in fig. 12i.

Finally, in fig. 11d,e and f. we plot the internal Q_{int} factors, which tell us about the losses of the resonator itself. In fig. 12d we see that the two designs from fig. 11a and c follow each other closely[13] with internal Q_{int} factors of $\approx 1.1 - 1.5 \cdot 10^4$, the 'nose' design from fig. 11a having slightly larger Q_{int} factor.

Fig. 12e and f and follow the same pattern of higher Q factors for the unbonded versions. The internal Q_{int} factors in fig. 12e follow each other more closely than the bonded and unbonded versions in fig. 12f. This shows a high internal unbonded Q_{int}, and a very low Q_{int} for the bonded resonator which ideally should not change. This means that the bonding has changed the inductance or capacitance of the resonator itself since $Q_{int} \propto C \propto 1/L$. Thus we assume that either the self capacitance fell or the inductance increased due to the wirebond overlapping the spiral turns[14] and thereby screening and lowering the resonators self capacitance while also increasing inductance.

Thus when comparing the different configurations, we clearly see that coupling our device hurts the Q_L factors. But when comparing the on-chip coupled resonators in fig. 12b and the off chip coupled resonators fig. 12c we actually get a marginally better loaded Q_L for the on chip resonators. Whether this is linked to the use of the on chip nanostrip connection to plunger gate for the on-chip resonators, rather than wirebond for the off-chip ones, is uncertain but plausible since it is rooted in the external Q_{ext} which is larger for the on-chip resonators than for the off-chip ones. It could however also be a matter of fabrication, that the on-chip resonators simply had less defects than the off-chip ones.

When comparing the loaded Q_L factors of the uncoupled resonators in fig. 12a with the uncoupled on-and off-chip resonators in fig. 12b and c, they are on par with the on-chip Q_Ls and generally worse than the inside out Tucuxis from fig. 11b. This could indicate that either the specific Tucuxi design is superior, or that the fabrication was more clean.

Regardless we still need to improve the loaded Q_L for the coupled chip resonators, as we would ideally want it to reach $Q_L \approx 10^3 - 10^4$ for our readout resonators in the low microwave frequency range, and in the order of 10^5 for strong coupling experiments[23]. To achieve this we are looking into using RIE (reactive ion etching) which is a method used for removing dangling bonds at the surface of

[13] Except for the single outlier at 1.2 GHz
[14] As described in fig. 11b caption.

the substrate thus decreasing substrate induced defects and thereby lowering photon losses [15]. Furthermore, an exciting next step, which would also maintain a pristine interface for both the quantum dot and resonator chips, could be trying to apply flip chip techniques. By creating the resonator in one step, we can decrease fabrication steps and obtain a cleaner resonator. We could then flip the resonator upside down, and sustaining it with indium pillars, hover the resonator device over the DQD, thereby omitting the wirebonds[24].

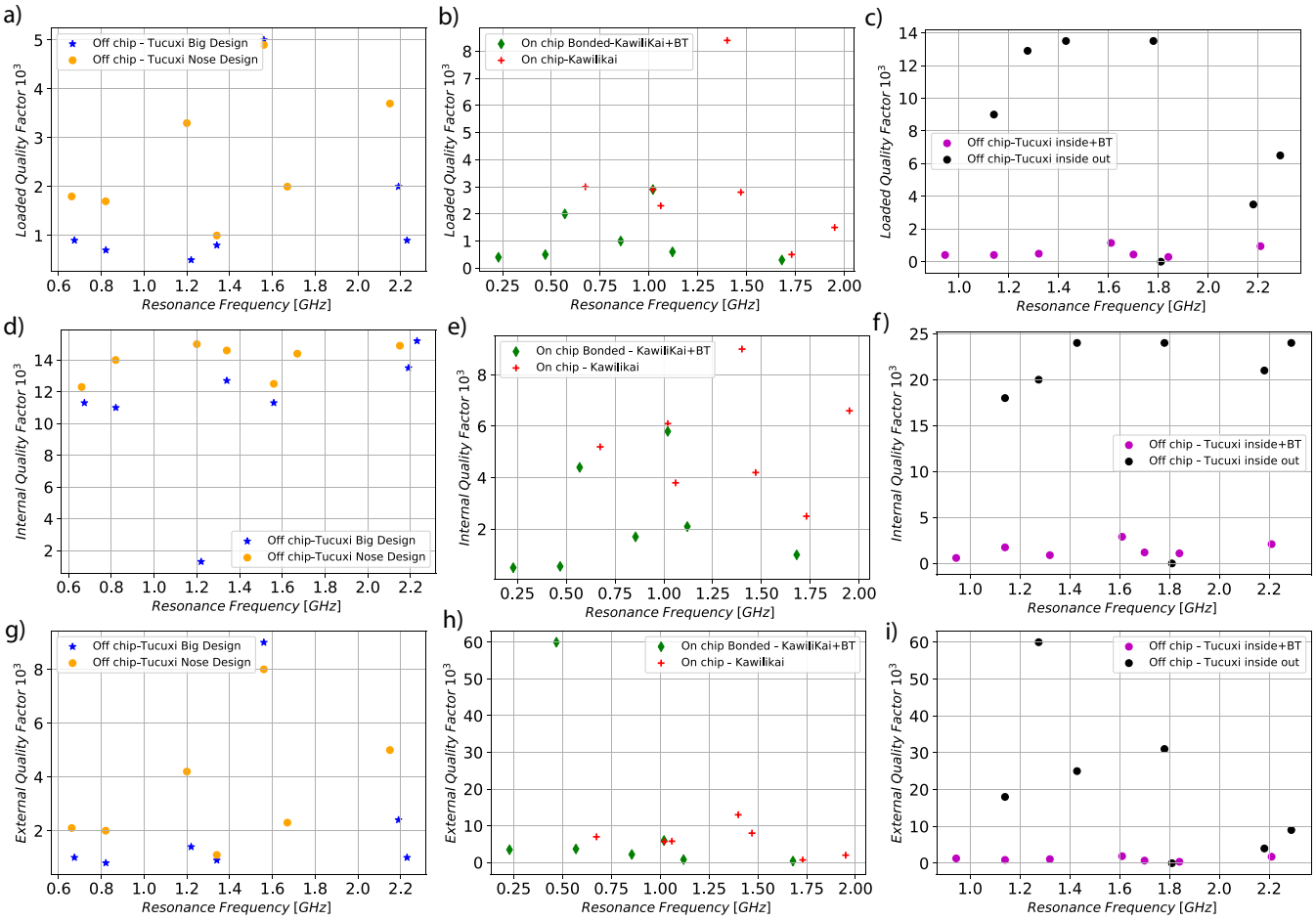

Figure 12: Extracted Q factors **a),d),g)**, are quality factors for two different Off chip Tucuxi designs, one with a nose peg as seen in fig. 11c, and one without the nose peg fig. 11a **b),e),h)** Quality factors for a bonded on-chip Fermats spiral resonator(Also dubbed Kawilikai) as seen in fig. 11d by wirebonding the top pad to a low pass filter bias tee., and the same device unbonded meaning the wirebonds to the double quantum dot device were pulled off.. **c),f),i)** Q factors belonging to a off-chip inductively coupled Tucuxi inside out resonator as seen in fig. 11b bonded to a bias tee low pass filter via the inner pad, and to a CEA leti double quantum dot device via the outer pad, and the same resonator device with the bonds pulled off.

6 Summary and outlook

6.1 Conlusion

We have thus designed, fabricated and tested a wide range of NW devices and resonators. A total of 9 out of 23 fabricated NW devices made it to testing and none of these 9 were in condition to be tuned to dots, nor work with the resonators. Concluding from the discussion in section 5.1.1 that our NW fabrication process needs a more systematic approach in order to achieve a higher yield.

As for the resonator arrays, we tested their dependency on temperature and magnetic field and can conclude that our feedline turns superconducting at $\approx 7.5K$, while resonances become stable at $\approx 1.2K$. We also confirmed that the resonators are resilient parallel magnetic fields, maintaining resonance features up till 3T.

Furthermore, we tested 4 different resonators in various configurations and extracted their Q factors. On background of the discussion in section 5.1.2, we report that coupling on-chip and and off-chip resonators to an external DQD will lower the loaded and external quality factor dramatically. We also observe that the internal Q_{int} falls in the case where you wirebond onto the the spiral located inside the resonator and thus effectively alter the resonator. Which encourages further investigation of designs that do not have pads inside the spiral like the one portrayed in fig. 12d. We compared two off-chip resonators with different 'feedline to resonator' coupling coastline lengths and observe that increasing this length gives us a higher loaded, internal and external factor. We report loaded Q_L factors in the order of 10^4 for uncoupled off-chip resonators and in the order $10^2 - 10^3$ for uncoupled on chip resonators. Concluding that we need to improve upon the fabrication in order to increase the quality factors if we are to achieve strong coupling [1, 25, 23] as discussed in section 5.1.2, but also that it is possible to utilize our resonators for charge sensing and readout [2].

6.2 Outlook

The first step after this thesis is to tune up a DQD and perform gate based sensing with the resonators. A final quarter wafer with 13 on chip NW devices is ready for the final fabrication steps. This wafer features a new resonator design, using the frame work of the Tucuxi resonators in fig. 11a and c, but with increased 'feedline to resonator' coupling coastline lenght, done by making multiple nose pegs instead of one like in fig. 11c. With this new design, we hope to achieve larger loaded Q_L factors. As for reaching the strong coupling regime, we plan to install an electric component called an isolater. It has the purpose of preventing our readout signal reflecting from the low temperature amplifier back to the device, thereby polluting the quantum states.

7 Acknowledgements

I want to thank, Fabio Ansaloni for teaching me how to measure, operate the fridge and generally how to be independent in the lab. Thanks to Anasua Chatterjee and Heorhii Bohuslavskyi for allways being helpful with whatever questions I may have had. Thanks to Dags Olsteins for teaching me how to use the micro manipulator and David Van Zanten for the fitting code. Thanks to Bertram Brovang, Morten Kjærgaard, Niels-Jakob Søe Loft, Sepher Ahmadi, Joost van der Heijden, Thorbjørn R. Rasmussen, Amber Heskes and Fabrizio Berrita for invaluable discussions, advice and favors. A huge thanks to Monica Mikkelsen for being the best. Thanks to Ferdinand Kuemmeth for letting me join the spinner gang and tolerating my antics. A huge thanks to all the wonderful people that welcomed me and made my short stay at qdev unforgettable! And last but not least I want to thank my beautiful girlfriend Lea and my son Costa, for providing infinite love and motivation.

References

[1] Guido Burkard et al. "Superconductor–semiconductor hybrid-circuit quantum electrodynamics". In: Nature Reviews Physics 2.3 (Jan. 2020), pp. 129–140.

[2] Y. -Y. Liu et al. Radio frequency reflectometry in silicon-based quantum dots. 2021. arXiv: 2012.14560 [cond-mat.mes-hall].

[3] P. Krantz et al. "A quantum engineer's guide to superconducting qubits". In: Applied Physics Reviews 6.2 (June 2019), p. 021318.

[4] many nerds. "Quantum Supremacy using a Programmable Superconducting Processor". In: Nature 574 (2019), pp. 505–510.

[5] Alexandre Blais et al. Circuit Quantum Electrodynamics. 2020. arXiv: 2005.12667 [quant-ph].

[6] Xuedong Hu, Yu-xi Liu, and Franco Nori. "Strong coupling of a spin qubit to a superconducting stripline cavity". In: Phys. Rev. B 86 (3 July 2012), p. 035314.

[7] Mircea Trif and Pascal Simon. "Braiding of Majorana Fermions in a Cavity". In: Physical Review Letters 122.23 (June 2019).

[8] N. Samkharadze et al. "High-Kinetic-Inductance Superconducting Nanowire Resonators for Circuit QED in a Magnetic Field". In: Phys. Rev. Applied 5 (4 Apr. 2016), p. 044004.

[9] Dong Liang, Juan Du, and Xuan P.A. Gao. "InAs Nanowire Devices with Strong Gate Tunability: Fundamental Electron Transport Properties and Application Prospects: A Review". In: Journal of Materials Science Technology 31.6 (2015). A Special Issue on 1D Nanomaterials, pp. 542–555.

[10] K. D. Petersson et al. "Circuit quantum electrodynamics with a spin qubit". In: Nature 490.7420 (Oct. 2012), pp. 380–383.

[11] Alexandre Blais et al. Circuit Quantum Electrodynamics. 2020.

[12] David Isaak Schuster. Circuit Quantum Electrodynamics Thesis. 2007. URL: https://rsl.yale.edu/sites/default/files/files/RSL_Theses/SchusterThesis.pdf,.

[13] X. Mi et al. "Circuit quantum electrodynamics architecture for gate-defined quantum dots in silicon". In: Applied Physics Letters 110.4 (2017), p. 043502.

[14] David M Pozar. Microwave engineering; 3rd ed. Hoboken, NJ: Wiley, 2005.

[15] A. Bruno et al. "Reducing intrinsic loss in superconducting resonators by surface treatment and deep etching of silicon substrates". In: Applied Physics Letters 106.18 (May 2015), p. 182601.

[16] T. Ihn. Semiconductor Nanostructures: Quantum States and Electronic Transport. OUP Oxford, 2010.

[17] W. G. van der Wiel et al. "Electron transport through double quantum dots". In: Rev. Mod. Phys. 75 (1 Dec. 2002), pp. 1–22.

[18] Deividas Sabonis et al. "Dispersive sensing in hybrid InAs/Al nanowires". In: Applied Physics Letters 115.10 (2019), p. 102601.

[19] Imtiaz Ahmed et al. "Radio-Frequency Capacitive Gate-Based Sensing". In: Physical Review Applied 10.1 (July 2018).

[20] Pobell .F. Matter and Methods at Low Temperatures. Springer, Berlin, Heidelberg., 1996.

[21] Y T Yemane et al. "Superconducting niobium titanium nitride thin films deposited by plasma-enhanced atomic layer deposition". In: Superconductor Science and Technology 30.9 (Aug. 2017), p. 095010.

[22] David Niepce, Jonathan Burnett, and Jonas Bylander. "High Kinetic Inductance NbN Nanowire Superinductors". In: Physical Review Applied 11.4 (Apr. 2019).

[23] N. Samkharadze et al. "High-Kinetic-Inductance Superconducting Nanowire Resonators for Circuit QED in a Magnetic Field". In: Physical Review Applied 5.4 (2016).

[24] D. Rosenberg et al. 3D integration and packaging for solid-state qubits. 2019. arXiv: 1906.11146 [quant-ph].

[25] N. Samkharadze et al. "Strong spin-photon coupling in silicon". In: 359.6380 (2018), pp. 1123–1127.

[26] Guillermo Gonzalez. Microwave Transistor Amplifiers (2nd Ed.): Analysis and Design. USA: Prentice-Hall, Inc., 1996. ISBN: 0132543354.

A Deriving Q_{ext} for two nodes

If we treat the resonator as having two nodes, one at the resonator input and one at the load, we can derive the total external Q_{ext}. The loaded quality factor is defined as as seen in equation **6.23** in Pozar [14].

$$Q_L = \frac{Q_{ext}Q_{int}}{Q_{ext} + Q_{int}} \tag{18}$$

Where the unloaded quality factor Q_{int} for parallel circuits is defined as

$$Q_{int} = \omega_0 Z_r C, \tag{19}$$

and the external Q_{ext} factors to be

$$Q_{ext,in} = \frac{2C_{in}}{\omega_0 Z_{in}}\ ,\ Q_{ext,out} = \frac{2C_{out}}{\omega_0 Z_{out}} \tag{20}$$

Where the external quality factors are related as the following

$$\frac{1}{Q_{ext}} = \frac{1}{Q_{ext,in}} + \frac{1}{Q_{ext,out}}, \tag{21}$$

$$Q_{ext} = \frac{Q_{ext,out}Q_{ext,in}}{Q_{ext,in} + Q_{ext,out}}, \tag{22}$$

which finally yields

$$Q_{ext} = \frac{2C_{in}C_{out}}{\omega_0(Z_{out}C_{in} - Z_{in}C_{out})}. \tag{23}$$

B Extracting Q_{ext}

We can find the insertion loss by using equation 2.52 in Pozar [14],

$$IL = -20log \mid S_{21} \mid, \tag{24}$$

$$IL = -10log \mid S_{21} \mid^2, \tag{25}$$

S_{21} for a 2 port impedance with the same transmission line impedance before port 1 and after port 2 is derived in Gonzalez [26] **1.6.25**

$$S_{21} = \frac{2Z_0}{Z + 2Z_0}, \tag{26}$$

Which for an admittance can be rewritten to

$$S_{21} = \frac{2Y_0}{Y + 2Y_0}. \tag{27}$$

,

$$S_{21} = \frac{2}{2 + \frac{Y}{Y_0}}. \tag{28}$$

As we have a parallel resonator with a shunt admittance Y looks like the following

$$Y = G + \frac{1}{j\omega L} + j\omega C, \tag{29}$$

Which can be approximated near the resonance frequency to the following, according to **6.71** in Pozar [14]

$$Y = G(1 + jQ_{int}\frac{2\Delta\omega}{\omega_0}). \tag{30}$$

Where $\Delta\omega = \frac{\pm\omega_0}{2Q_L}$ at the FWHM at the resonance center frequency. Before inserting back into our S_{21} we realize $\frac{G}{G_0}$ is one over our coupling factor g (in pozar atleast **eq. 6.76** [14]). Which is defined as the following for parallel circuits.

$$g = \frac{G_0}{G} = \frac{Q_{int}}{Q_{ext}}. \tag{31}$$

.

We thus get

$$S_{21} = \frac{2}{2 + \frac{Q_{ext}}{Q_{int}}(1 + jQ_{int}\frac{2\Delta}{\omega_{int}})}, \tag{32}$$

which also can be written as

$$S_{21} = \frac{\frac{Q_{int}}{Q_{ext}}}{\frac{Q_{int}}{Q_{ext}} + (1 + jQ_{int}\frac{2\Delta}{\omega_0})}, \tag{33}$$

Using the expression for Q_L we can rewrite to

$$S_{21} = \frac{\frac{Q_L}{Q_{ext}}}{1 + (Q_L 2\frac{\Delta\omega}{\omega_0})}. \tag{34}$$

Thus S_{21} is now a function of the loaded Q_L factor , and internal Q_{int} factor. Which can be used to model an ideal resonance peak. Squaring this expression and rewriting into terms of the internal Q_{int}

and Q_L, and inserting into eq. 25 we get the insertion loss.

$$IL = -10log\frac{(1-\frac{Q_L}{Q_{int}})^2}{1+(Q_L 2\frac{\Delta\omega}{\omega_0})^2} \tag{35}$$

Which we then can use to extract the Q_{ext}. So since we can get the loaded quality factor Q_L from the FWHM bandwidth and the unloaded quality factor Q_{int} by measuring the IL, we can just use

$$Q_L = \frac{Q_{ext}Q_{int}}{Q_e + Q_{int}}, \tag{36}$$

which with a few steps can be rewritten as

$$Q_{ext} = \frac{Q_L Q_{int}}{Q_L - Q_{int}}. \tag{37}$$

We furthermore know from question 5, that

$$Q_{ext} = \frac{Q_L Q_{int}}{Q_L - Q_{int}}. \tag{38}$$

Thus if we again assume that external quality factor at the feedline is $Q_{ext,in}$ and at the other end is $Q_{ext,out}$ are the same thus we get that

$$Q_{ext} = 2\frac{Q_L Q_{int}}{Q_L - Q_{int}}. \tag{39}$$

Inserting the expression for Q_{int} first, we get

$$Q_{ext} = 2\frac{Q_L\frac{Q_L}{1-10^{\frac{-IL\omega_0}{20}}}}{Q_L(1-\frac{1}{1-10^{\frac{-IL\omega_0}{20}}})}, \tag{40}$$

$$Q_{ext} = 2\frac{Q_L}{10^{\frac{-IL\omega_0}{20}}}, \tag{41}$$

finally inserting the Q_L

$$Q_{ext} = \frac{\omega_0}{\Delta\omega_{3dB}\cdot 10^{\frac{-IL\omega_0}{20}}}. \tag{42}$$

C Micro-manipulator cheat sheet

The 'QDev cleanroom staff', which usually trains students on the various fabrication tools, does not provide training for the micro-manipulator. It is therefore left as a job for members of the students research group. I will thus include a guide for my academic peers to use, as preparation before starting their training.

1. Initializing and setting up.
    - Equip shoecovers and latex gloves.
    - Turn on microscope lights and camera software. If stage is not at home press ”home” on the stage controller.
    - Deposit device chip and nanowire growth substrate in the center of the stage.
2. Setting the stage
    - Move stage to growth substrate. Optimize microscope focus with the 10x lens , proceed zooming until 100x lens and focus has been reached - save position on stage controller.
    - Move the stage to desired nanowire drop-off spot WITHOUT adjusting microscope focus, but instead focusing ONLY with the z-axis controller on the stage controller. When focus and drop-off is found - save position on stage controller. This is done to maintain focus on the substrate.
3. Needle height positioning.
    - Revert lens from 100x to 25x and with a tweezer attach needle in Transferman arm. Use 'Transferman' controller to set the arm to maximum achievable z-heigth.
    - Manually place needle-arm under microscope light and over substrate. Lower needle manually to approximatly 1mm over substrate.
    - Find the needle tip and center it on the screen, by playing with focus and slowly lowering the needle. Increase zoom to 50x, focus, lower needle until full focus is reached again. Repeat with 100x untill needle is just above the substrate - save position as ”1” on the 'Transferman'.
    - Lift needle from just above the substrate to approximatly 500μm from that position - save lifted position as ”2” on ”Transferman”
4. Harvesting

- Now we are ready for harvesting. Find a suitable nanowire on the substrate, pick it up, and bring needle up to the saved lifted position.
- Use the saved stage drop-off position to take you directly to the drop off. Lower arm to substrate and Place wire, then push it around carefully until satisfactory position is archieved.
- Bring to lifted postion and return to substrate by using saved subtrate stage position.
- Rinse and repeat.

5. When done

    - Bring lens back to 10x
    - Remove needle and dispose there off safely into appropriate bin.
    - Set stage to home and turn of lights.

Picking up nanowires is easier said than done. several things can go wrong. If too many wires accumulate on your needle you may not be able to get any off the needle again, as they will attract each other; And in the case you get them off you will end with too many bunched up in a ball. Breakage of wires easily occurs. Scratching of bottom gates and substrates is imminent if not careful. These things can only be avoided with patience and time spent at the Micro-manipulator. Slow and steady wins the race.